

Dynamical characterization of quadrupole topological phases in superconducting circuitsChaohua Wu^{1,2}, Xin Guan^{1,2}, Jingtao Fan^{1,2,*}, Gang Chen^{1,2,3,†} and Suotang Jia^{1,2}¹*State Key Laboratory of Quantum Optics and Quantum Optics Devices, Institute of Laser Spectroscopy, Shanxi University, Taiyuan 030006, China*²*Collaborative Innovation Center of Extreme Optics, Shanxi University, Taiyuan, Shanxi 030006, China*³*Collaborative Innovation Center of Light Manipulations and Applications, Shandong Normal University, Jinan 250358, China*

(Received 14 May 2021; accepted 20 July 2021; published 3 August 2021)

The recent experimental realization of a programmable two-dimensional square superconducting qubit array opens a new avenue for quantum simulation with qubits [Science 372, 948 (2021)]. Here, we present an experimentally feasible method to achieve two-dimensional superconducting qubit lattice with tunable coupling strengths. A configuration with higher-order topological phases is constructed, featuring topologically protected boundary states in lower dimension (corner states). We show that the quadrupole topological phases can be effectively characterized by the dynamics of the single-excitation quantum state. Moreover, we also explore the detection and dynamics of the corner modes in our qubit lattice system. Particularly, we propose an effective scheme to realize quantum information transfer via the corner states. Our work suggests that superconducting circuits systems are a fertile platform to study novel topological quantum phases and may shed light on the ongoing exploration of topologically protected quantum information processing.

DOI: [10.1103/PhysRevA.104.022601](https://doi.org/10.1103/PhysRevA.104.022601)**I. INTRODUCTION**

Superconducting circuits, as a scalable system for quantum computation [1,2], have achieved great experimental progress in the past few years. Particularly, this system has now become one of the promising platforms for studying quantum simulation [3,4], especially quantum many-body systems [5]. Compared with other quantum simulation systems, such as cold atoms [6] and photonics [7], the superconducting qubits may be a qualified candidate for its easy manipulation, detection, flexible tunability, and fine controllability. In fact, a wide range of many-body physics has been studied in such simulators, including the extended Bose-Hubbard model [8–10], many-body localization [11–14], as well as dynamical phase transitions [15]. In addition, superconducting qubit systems are also advantageous in the research of topological physics, such as topological quantum walks [16,17], topological state transfer [18–20], and other topological concepts [21–23]. Recently, the topological magnon insulator states have been observed in a superconducting qubit chain with tunable qubit couplings [24]. Remarkably, a recent experimental observation of quantum walks on a programmable two-dimensional (2D) square superconducting qubit lattice provides a new platform for quantum information processing and quantum simulation [25]. The 2D qubit system plays a crucial role in exploring exotic physical phenomena [26–29] and implementing quantum information [30,31].

One of the hallmark features of conventional topological insulators is the topologically protected boundary states (such as edge and surface states) with dimensions one lower than

that of the bulk system [32,33]. These states are guaranteed by the bulk-boundary correspondence, which is characterized by the bulk topological invariants (quantized bulk dipole moments). Recently, a novel class of topological phases, called higher-order topological insulators (HOTIs), were proposed by generalizing the fundamental relationship between the Berry phase and quantized polarization, from dipole to multipole moments [34–36]. The key feature of HOTIs is their ability to support topological states with dimensions two or more lower than those of the bulk. For example, a quantized bulk quadrupole moment in a 2D system leads to the presence of gapped zero-energy states localized at the zero-dimensional (0D) corners (corner states), which is called a second-order topological insulator. Motivated by the potential applications for designing novel robust optical devices, topological lasers, as well as quantum computing, the HOTI has garnered substantial interest in recent years [37–47].

In this paper, we demonstrate simulation of quadrupole topological phases in a 2D superconducting qubit lattice with tunable coupling strengths, which is analogue to the Benalcazar-Bernevig-Hughes (BBH) model. The nontrivial quadrupole phase supports 0D corner states that are guaranteed by the quantized bulk quadrupole moment. We show that the quadrupole topological phases can be effectively characterized by the dynamics of the single-excitation quantum state. Specifically, such dynamical dependent quantities take zero for the trivial quadrupole phase and finite for the nontrivial quadrupole phase. Moreover, we also explore the detection and dynamics of the corner modes in our qubit lattice system. Furthermore, we propose an effective scheme to realize transfer of the corner states. Our work suggests that the superconducting circuits system is a fertile platform to study novel topological quantum phases and may shed light on the ongoing exploration of topologically protected quantum information processing.

*bkxyft@163.com

†chengang971@163.com

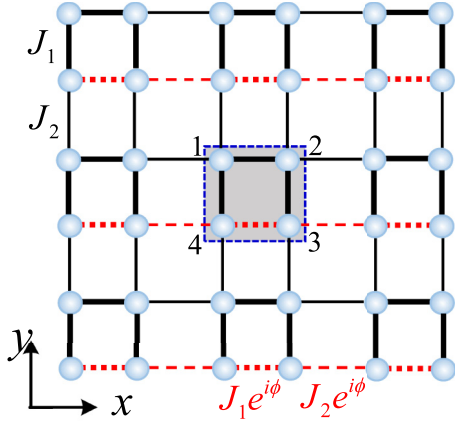


FIG. 1. (a) Schematic of 2D square qubit lattice with nearest-neighbor couplings. Thick (thin) lines denote couplings with strength J_1 (J_2). The red-dashed lines indicate a phase factor $e^{i\phi}$ on the coupling, which introduces a flux ϕ per unit cell.

II. MODEL AND HAMILTONIAN

We consider a 2D square qubit lattice consisting of $N \times N$ capacitively coupled qubits, as shown in Fig. 1. Each unit cell contains four sites with only the nearest-neighbor coupling. The coupling strengths J_1 (thick lines) and J_2 (thin lines) describe coupling strengths between qubits within the same unit cell and those that belong to adjacent unit cells, respectively. Particularly, each plaquette, a square of any four adjacent qubits within or between unit cells, contains a single coupling term that carries an extra phase shift ϕ [red lines in Fig. 1], which amounts to the generation of a synthetic magnetic flux ϕ threading the plaquette. The Hamiltonian reads

$$H = \sum_{m,n} (J_1 \sigma_{m,n-1}^\dagger e^{i\phi\delta_m} \sigma_{m,n} + J_2 \sigma_{m,n}^\dagger e^{i\phi\delta_m} \sigma_{m,n+1} + J_1 \sigma_{m-1,n}^\dagger \sigma_{m,n} + J_2 \sigma_{m,n}^\dagger \sigma_{m+1,n}) + \text{H.c.}, \quad (1)$$

$$\begin{aligned} \tilde{H} &= U^\dagger H U + i \frac{dU^\dagger}{dt} U \\ &= \sum_{m,n} g_x^{m,n} (\sigma_{m,n-1}^+ \sigma_{m,n}^- e^{-i\Delta_x^{m,n}} \exp[-i\alpha_{m,n-1} \cos(v_{m,n-1}t + \theta_{m,n-1})] \exp[i\alpha_{mn} \cos(v_{mn}t + \theta_{mn})] + \text{H.c.}) \\ &\quad + \sum_{m,n} g_y^{m,n} (\sigma_{m-1,n}^+ \sigma_{m,n}^- e^{-i\Delta_y^{m,n}} \exp[-i\alpha_{m-1,n} \cos(v_{m-1,n}t + \theta_{m-1,n})] \exp[i\alpha_{mn} \cos(v_{mn}t + \theta_{mn})] + \text{H.c.}), \end{aligned} \quad (6)$$

where $\Delta_x^{m,n} = \omega_{m,n} - \omega_{m,n-1}$ and $\Delta_y^{m,n} = \omega_{m,n} - \omega_{m-1,n}$. We assume $\Delta_x^{m,n} = v_{mn}$ ($-v_{mn}$) for odd (even) n , and $\Delta_y^{m,n} = v_{mn}$ ($-v_{mn}$) for odd (even) m . Then, using the Jacobi-Anger identity

$$\exp[i\alpha \cos(vt + \theta)] = \sum_{l=-\infty}^{\infty} i^l \mathcal{J}_l(\alpha) e^{il(vt + \theta)}, \quad (7)$$

with $\mathcal{J}_l(\alpha)$ being the l th Bessel function of the first kind, and applying the rotating-wave approximation by neglecting the high-order oscillation terms, the effective Hamiltonian of the

system becomes

$$\tilde{H}_{\text{eff}} = \sum_{m,n} (\tilde{g}_x^{m,n} \sigma_{m,n-1}^+ \sigma_{m,n}^- + \tilde{g}_y^{m,n} \sigma_{m-1,n}^+ \sigma_{m,n}^-) + \text{H.c.}, \quad (8)$$

with the effective coupling strengths

$$\begin{aligned} \tilde{g}_x^{m,n} &= g_x^{m,n} \mathcal{J}_0(\alpha_{m,n-1}) \mathcal{J}_1(\alpha_{mn}) e^{\pm i(\theta_{mn} \pm \pi/2)}, \\ \tilde{g}_y^{m,n} &= g_y^{m,n} \mathcal{J}_0(\alpha_{m-1,n}) \mathcal{J}_1(\alpha_{mn}) e^{\pm i(\theta_{mn} \pm \pi/2)}, \end{aligned} \quad (9)$$

where “ \pm ” denotes n (m) is odd and even in $\tilde{g}_x^{m,n}$ ($\tilde{g}_y^{m,n}$), respectively. It follows from Eq. (9) that we can conveniently

where the sum of (m, n) goes over all qubits and $\sigma_{m,n}^\dagger$ ($\sigma_{m,n}$) is the raising (lowering) operator of qubit $Q_{m,n}$ defined on a lattice site $(x = ma, y = nb)$, where a and b are the lattice spacings, and m and n are integers. $\delta_m = 0$ ($\delta_m = 1$) when m is odd (even). H.c. is the Hermitian conjugate. We take $\hbar = 1$ throughout the paper for simplicity.

In the following, we provide an experimental feasible protocol to achieve the effective Hamiltonian (1). For a standard 2D square qubit lattice, the Hamiltonian can be described by

$$\begin{aligned} \mathcal{H} &= \sum_{m,n} \frac{\omega_{mn}}{2} \sigma_{m,n}^z + \sum_{m,n} g_x^{m,n} (\sigma_{m,n-1}^+ \sigma_{m,n}^- + \text{H.c.}) \\ &\quad + \sum_{m,n} g_y^{m,n} (\sigma_{m-1,n}^+ \sigma_{m,n}^- + \text{H.c.}), \end{aligned} \quad (2)$$

where $\sigma_{m,n}^z$ is the Pauli operator of qubit $Q_{m,n}$, ω_{mn} is the transition frequency, and $g_x^{m,n}$ and $g_y^{m,n}$ are the static coupling strengths. Generally, the qubit-frequency differences of adjacent transmon qubits and their coupling strengths are fixed and not adjustable. To achieve fully tunable coupling strengths, one can apply an ac magnetic flux to periodically modulate the qubit frequencies [48–50], that is

$$\omega_{mn}(t) = \bar{\omega}_{mn} + \epsilon_{mn} \sin(v_{mn}t + \theta_{mn}). \quad (3)$$

Here, $\bar{\omega}_{mn}$ is the mean operating frequency with $m, n = 1, \dots, N$. ϵ_{mn} , v_{mn} , and θ_{mn} are the modulation amplitude, frequency, and phase, respectively. By defining a rotating frame through $U = U_1 \cdot U_2$ with

$$U_1 = \exp\left(-i \sum_{m,n} \frac{\omega_{mn}}{2} \sigma_{m,n}^z t\right), \quad (4)$$

$$U_2 = \exp\left[i \sum_{m,n} \sigma_{m,n}^z \frac{\alpha_{mn}}{2} \cos(v_{mn}t + \theta_{mn})\right], \quad (5)$$

where $\alpha_{mn} = \epsilon_{mn}/v_{mn}$, we obtain the transformed Hamiltonian

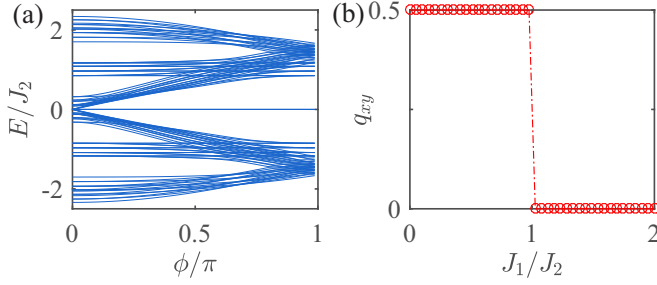


FIG. 2. (a) Energy spectrum vs ϕ with $J_1/J_2 = 0.2$ and $N = 10$. (b) Bulk quadrupole polarization vs J_1/J_2 .

tune the effective coupling strengths by changing $\alpha_{m,n}$ of the external modulation. Note that there is a phase factor in each coupling which can be used to produce effective magnetic flux in a square qubit lattice [51,52]. By choosing appropriate parameters ($\{\alpha_{mn}, \theta_{mn}\}$), the Hamiltonian (1) can be realized according to Eq. (8).

Equation (1) describes an interacting spin (qubit) lattice model, where multiple excitations behave like hard-core bosons. For single-excitation case, the Hamiltonian (1) reduces to a noninteracting model. In the present work we focus on the single-qubit excitation case, i.e., one of the qubits is excited to the excited state $|e\rangle$ and the others stay in the ground state $|g\rangle$. Due to the conservation of qubit excitation number, the qubit lattice will stay in single-excitation space during the entire dynamical evolution.

The key merit of our system is the flexible tunability of the coupling parameters, which provides a fertile ground for studying topological physics. In Fig. 2(a) we plot the energy spectrum for various ϕ with $J_1/J_2 = 0.2$. It can be seen that there is a band gap for flux $0 < \phi < \pi$. This band gap shrinks as $\phi \rightarrow 0$ and completely closes at $\phi = 0$. In fact, the lattice with zero flux ($\phi = 0$) can be viewed as a 2D analog of the Su-Schrieffer-Heeger (SSH) model [53,54]. Since the band gap disappears, the 2D SSH model does not feature any robust corner states. However, for $\phi = \pi$, Eq. (1) reduces to a spin-ersion BBH model [34,35], which is a quadrupole HOTI. Intriguingly, this model hosts robust zero-energy corner states, guaranteed by a quantized bulk quadrupole moment [34,55]. In Fig. 2(b), the quantized bulk quadrupole moment q_{xy} is shown as a function of J_1/J_2 , giving

$$q_{xy} = \begin{cases} 1/2, & \text{topology } (J_1/J_2 < 1) \\ 0, & \text{trivial } (J_1/J_2 > 1). \end{cases} \quad (10)$$

In the following we focus on the simulation and detection of the quadrupole topological phases in a BBH-type 2D superconducting qubit lattice. We show that the quadrupole phases are tightly related to the dynamics of quantum state in such 2D qubit lattice. Moreover, a scheme to transfer the corner states is presented.

III. DYNAMICAL DETECTION OF THE QUADRUPOLE PHASES

In general, the topological invariant (winding number) can be extracted from a time-dependent quantity, that is, the mean chiral displacement (MCD) [56], which has been measured

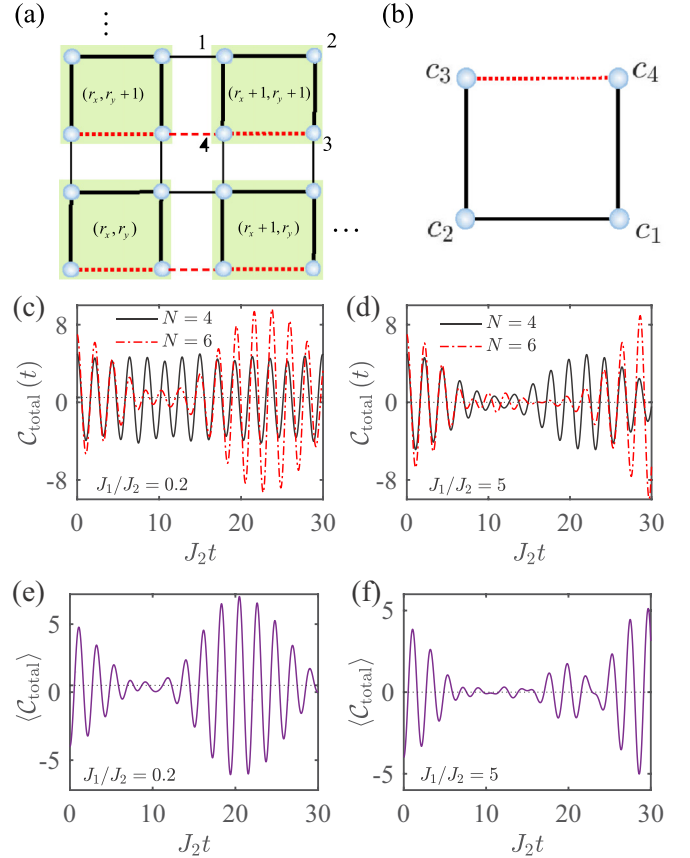


FIG. 3. (a) Schematic of qubit lattice in unit-cell coordinate. (b) Schematic of four-qubit plaquette. The red-dashed line denotes the negative coupling strength, i.e., carrying $\phi = \pi$ phase. (c, d) The dynamics of $C_{\text{total}}(t)$ with $J_1/J_2 = 0.2$ (c) and $J_1/J_2 = 5$ (d), respectively. The black solid (red-dashed) lines denote $N = 4$ ($N = 6$). (e, f) The dynamics of $\langle C_{\text{total}} \rangle$ in the presence of qubit coupling imperfection with $J_1/J_2 = 0.2$ (e) and $J_1/J_2 = 5$ (f), respectively. Here $\langle \cdot \rangle$ denotes the averaged value over 50 independent disorder configurations. The disorder strength is chosen by $W/J_2 = 0.1$.

experimentally in a photonic quantum walk [57], cold atom [58], and superconducting qubit chain [24].

For the quadrupole phases in our 2D qubit lattice system, we introduce the chiral displacement operator [59]

$$\hat{C} = \sum_{\mathbf{r}, \mu} r_x r_y \Gamma_\mu \hat{P}_{\mathbf{r}, \mu}, \quad (11)$$

which can be regarded as an extension of the MCD in Ref. [24]. Here, $\mathbf{r} = (r_x, r_y)$ is the position of the unit cell, and $\mu = 1, 2, 3, 4$ characterizes the sublattice in each unit cell, as shown in Fig. 3(a). $\Gamma_\mu = (-1)^\mu$ is the eigenvalue of the chiral operator and $\hat{P}_{\mathbf{r}, \mu} = |e\rangle_{\mathbf{r}, \mu} \langle e|$. The dynamics of the MCD is described by

$$\mathcal{C}(t) = \langle \psi(t) | \hat{C} | \psi(t) \rangle, \quad (12)$$

where $|\psi(t)\rangle$ is the state vector at time t . The long-time average of $\mathcal{C}(t)$ is $\bar{\mathcal{C}} = \lim_{T \rightarrow \infty} (1/T) \int_0^T \mathcal{C}(t) dt$.

Note that $\mathcal{C}(t)$ is sensitive to the choice of the initial state. To be concrete, let us denote $C_\mu^{i,j}(t)$ as the MCD obtained from the state initialized at the sublattice μ of the unit cell (i, j) . It

is found that the MCD which can correctly characterize the topological quadrupole phases is simply the addition of the following two independent trajectories:

$$\mathcal{C}_{\text{total}}(t) = \mathcal{C}_1^{r_x+1, r_y}(t) + \mathcal{C}_3^{r_x, r_y+1}(t). \quad (13)$$

More numerical results for other different initial states are given in the Appendix.

To demonstrate the validity of Eq. (13) in describing the quadrupole phases, we first consider the single-particle dynamics in two limiting cases—the trivial ($J_1 \neq 0, J_2 = 0$) and the nontrivial ($J_1 = 0, J_2 \neq 0$) ones. In these two cases, the dynamics is limited to four lattice sites labeled c_1, c_2, c_3 , and c_4 , as shown in Fig. 3(b), which can be solved analytically. In the single-excitation basis, the Hamiltonian can be written as

$$H_{\text{four}} = \begin{pmatrix} 0 & 1 & 0 & 1 \\ 1 & 0 & 1 & 0 \\ 0 & 1 & 0 & -1 \\ 1 & 0 & -1 & 0 \end{pmatrix}, \quad (14)$$

where the coupling strength is set to 1. The eigenenergies of H_{four} are straightforwardly obtained as $\varepsilon_{1,2} = -\sqrt{2}$ and $\varepsilon_{3,4} = \sqrt{2}$. The corresponding eigenstates are given by $\Phi_1 = (1/2, -1/\sqrt{2}, 1/2, 0)^T$, $\Phi_2 = (1/2, 0, -1/2, -1/\sqrt{2})^T$, $\Phi_3 = (1/2, 1/\sqrt{2}, 1/2, 0)^T$, and $\Phi_4 = (1/2, 0, -1/2, 1/\sqrt{2})^T$.

Supposing the initial state is $|\psi(0)\rangle = (\psi_1, \psi_2, \psi_3, \psi_4) = \sum_i f_i \Phi_i$, with $f_i = \langle \Phi_i | \psi(0) \rangle$. The wave function at time t can be written as

$$\begin{aligned} |\psi(t)\rangle &= e^{-iH_{\text{four}}t} |\psi(0)\rangle \\ &= \sum_i f_i e^{-i\varepsilon_i t} \Phi_i \\ &= \begin{pmatrix} \psi_1 \cos(\sqrt{2}t) - \frac{i}{\sqrt{2}}(\psi_2 + \psi_4) \sin(\sqrt{2}t) \\ \psi_2 \cos(\sqrt{2}t) - \frac{i}{\sqrt{2}}(\psi_1 + \psi_3) \sin(\sqrt{2}t) \\ \psi_3 \cos(\sqrt{2}t) - \frac{i}{\sqrt{2}}(\psi_2 - \psi_4) \sin(\sqrt{2}t) \\ \psi_4 \cos(\sqrt{2}t) - \frac{i}{\sqrt{2}}(\psi_1 - \psi_3) \sin(\sqrt{2}t) \end{pmatrix}. \end{aligned} \quad (15)$$

Then the excitation probability for each qubit is given as

$$\begin{aligned} P_{c_1}(t) &= |\psi_1|^2 \cos^2(\sqrt{2}t) + \frac{|\psi_2 + \psi_4|^2}{2} \sin^2(\sqrt{2}t) \\ &\quad - \frac{1}{\sqrt{2}} \sin(2\sqrt{2}t) \text{Im}[\psi_1(\psi_2^* + \psi_4^*)], \end{aligned} \quad (16)$$

$$\begin{aligned} P_{c_2}(t) &= |\psi_2|^2 \cos^2(\sqrt{2}t) + \frac{|\psi_1 + \psi_3|^2}{2} \sin^2(\sqrt{2}t) \\ &\quad - \frac{1}{\sqrt{2}} \sin(2\sqrt{2}t) \text{Im}[\psi_2(\psi_1^* + \psi_3^*)], \end{aligned} \quad (17)$$

$$\begin{aligned} P_{c_3}(t) &= |\psi_3|^2 \cos^2(\sqrt{2}t) + \frac{|\psi_2 - \psi_4|^2}{2} \sin^2(\sqrt{2}t) \\ &\quad - \frac{1}{\sqrt{2}} \sin(2\sqrt{2}t) \text{Im}[\psi_3(\psi_2^* - \psi_4^*)], \end{aligned} \quad (18)$$

$$\begin{aligned} P_{c_4}(t) &= |\psi_4|^2 \cos^2(\sqrt{2}t) + \frac{|\psi_1 - \psi_3|^2}{2} \sin^2(\sqrt{2}t) \\ &\quad - \frac{1}{\sqrt{2}} \sin(2\sqrt{2}t) \text{Im}[\psi_4(\psi_1^* - \psi_3^*)]. \end{aligned} \quad (19)$$

According to Eqs. (16)–(19), one can obtain the MCD. For the trivial case ($J_1 \neq 0, J_2 = 0$), these four qubits are in the same unit cell [e.g., (r_x, r_y)] by taking correspondence $c_1 \rightarrow 1, c_2 \rightarrow 2, c_3 \rightarrow 3$, and $c_4 \rightarrow 4$. The MCD is given as $\mathcal{C}^{\text{triv}}(t) = \sum_{\mu} (-1)^{\mu} r_x r_y P_{c\mu}$. For two initial states $|\psi_1(0)\rangle = |\text{eggg}\rangle = (1, 0, 0, 0)$ located at unit cell $(r_x + 1, r_y)$ and $|\psi_3(0)\rangle = |\text{gggg}\rangle = (0, 0, 1, 0)$ located at unit cell $(r_x, r_y + 1)$, the total MCD is obtained as

$$\begin{aligned} \mathcal{C}_{\text{total}}^{\text{triv}}(t) &= \mathcal{C}_1^{\text{triv}}(t) + \mathcal{C}_3^{\text{triv}}(t) \\ &= [(r_x + 1)r_y + r_x(r_y + 1)] \cos 2\sqrt{2}t, \end{aligned} \quad (20)$$

yielding $\bar{\mathcal{C}}_{\text{total}}^{\text{triv}} = 0$. Obviously, it is independent of the initial state. However, for the nontrivial case ($J_1 = 0, J_2 \neq 0$), the four qubits are in different unit cells. The correspondence between Figs. 3(a) and 3(b) is as follows: $c_1 \rightarrow [(r_x + 1, r_y), 1], c_2 \rightarrow [(r_x, r_y), 2], c_3 \rightarrow [(r_x, r_y + 1), 3]$, and $c_4 \rightarrow [(r_x + 1, r_y + 1), 4]$. Here, $[(r_x, r_y), \mu]$ denotes the sublattice μ in the unit cell (r_x, r_y) . In this case, the MCD is $\mathcal{C}^{\text{topo}}(t) = \sum_{\mu} (-1)^{\mu} r_x r_y P_{c\mu} + [(r_x + r_y + 1)P_{c_4} - r_y P_{c_1} - r_x P_{c_3}]$. For the initial states $|\psi_1(0)\rangle$ and $|\psi_3(0)\rangle$, we have

$$\begin{aligned} \mathcal{C}_{\text{total}}^{\text{topo}}(t) &= \mathcal{C}_1^{\text{topo}}(t) + \mathcal{C}_3^{\text{topo}}(t) \\ &= \frac{1}{2} - (2r_x r_y + r_x + r_y + \frac{1}{2}) \cos 2\sqrt{2}t. \end{aligned} \quad (21)$$

Taking the long-time average, we obtain $\bar{\mathcal{C}}_{\text{total}}^{\text{topo}}(t) = 0.5$. The above analysis indicates that the dynamics of the single-excitation state is a qualified candidate to distinguish the topological nontrivial and trivial quadrupole phases. That is, $\bar{\mathcal{C}}_{\text{total}} = 0$ with $\{J_1 \neq 0, J_2 = 0\}$, while $\bar{\mathcal{C}}_{\text{total}} = 0.5$ with $\{J_1 = 0, J_2 \neq 0\}$.

We now provide numerical simulation for general cases. In Figs. 3(c) and 3(d), we plot $\mathcal{C}_{\text{total}}(t)$ for $J_1/J_2 = 0.2$ and $J_1/J_2 = 5$, respectively. It can be seen that $\mathcal{C}_{\text{total}}(t)$ oscillates around 0.5 ($\bar{\mathcal{C}}_{\text{total}} = 0.5$) in the nontrivial quadrupole phase [Fig. 3(c)], while it oscillates around zero ($\bar{\mathcal{C}}_{\text{total}} = 0$) in the trivial quadrupole phase [Fig. 3(d)].

The quadrupole topological phases are protected by the quantized bulk quadrupole moment and are robust to perturbations. To show the robustness of the MCD, we consider the imperfect qubit couplings. Specifically, we assume that the intra and inter uniting cell coupling strengths have the form of $J'_{1mn} = J_1 + W\eta_{mn}$ and $J'_{2mn} = J_2 + W\eta_{mn}$, where W denotes the disorder strength, and η_{mn} is an independent random real number chosen uniformly from the range $[-0.5, 0.5]$. In Figs. 3(e) and 3(f), we plot the dynamics of the disorder-averaged $\mathcal{C}_{\text{total}}(t)$ by choosing 50 samples of $\{J'_{1mn}, J'_{2mn}\}$ for trivial and nontrivial cases, respectively. The results clearly show that $\langle \mathcal{C}_{\text{total}} \rangle$ still oscillates at around about 0.5 and zero for weak disorder.

IV. TOPOLOGICAL CORNER STATE AND ITS TRANSFER

Having discussed the characterization of the quadrupole phases through the dynamics of quantum state, we now move on to the research of the corner states. Due to the topological properties of these corner states, information can be trapped at the corners of the system, which will be robust against weak disorder, making it a potential candidate for information processing. However, the corner states, as with other topo-

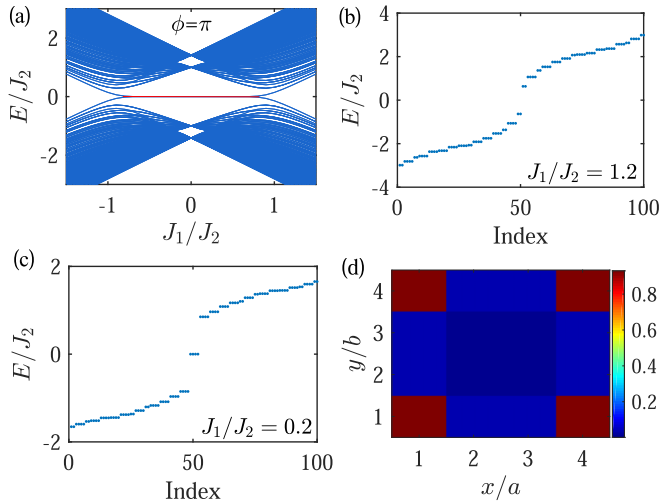


FIG. 4. (a) Energy spectrum vs J_1/J_2 with $\phi = \pi$. (b, c) Energy spectrum for $\phi = \pi$ and $N = 10$ with $J_1/J_2 = 1.2$ (b) and $J_1/J_2 = 0.2$ (c), respectively. (d) The collective distribution wave functions of the corner states (the four zero-energy modes) for 4×4 lattice. The other parameters are the same as those in (c).

logical modes, are well isolated from each other even in the presence of disorder, making it difficult for them to overlap. On the other hand, the corner states may hybridize due to finite system size. Consequently, it is meaningful to realize the exchange of information among the corner states. In the following, we first show the detection of the corner states and then propose an effective scheme to transfer each corner state.

A. Topological corner states

In Fig. 4(a) we plot the energy spectrum as a function of J_1/J_2 for $\phi = \pi$. It is found that some quasidegenerate midgap modes, separating the upper and lower bulk bands, appear in the nontrivial quadrupole phase region where $\phi = \pi$ and $|J_1/J_2| < 1$. Specifically, we show the energy spectrum for $J_1/J_2 = 1.2$ and $J_1/J_2 = 0.2$, as shown in Figs. 4(b) and 4(c), respectively. It follows that there exists four energy-degenerate zero-energy modes when $J_1/J_2 = 0.2$. These midgap modes represent nothing but the corner states localized at the corners of the 2D lattice [shown in Fig. 4(d)]. This property is well manifested in the qubit dynamics within a subspace spanned by the single-excitation states $|\Psi_{i,j}\rangle = \sigma_{i,j}^\dagger |G\rangle$, where $|G\rangle = |gg \cdots g\rangle$ is the ground state. Figure 5 shows the time evolution of the excited-state population for $J_1/J_2 = 1.2$ and $J_1/J_2 = 0.2$, respectively. In these figures the initial states are set to be $\sigma_{4,1}^\dagger |G\rangle$. It can be seen from Figs. 5(a1)–5(a3) that the initial wave packet spreads over the whole lattice. However, for the topological nontrivial case shown in Figs. 5(b1)–5(b3), the excited-state populations are, although changing over time, well localized in the lattice corners. Interestingly, the qubit flipping occurs only at three—the initially excited one and its two nearest neighbors—out of the four corners. The detailed dynamics of the four corners are plotted in Fig. 6(a). This phenomenon can be understood by investigating the spec-

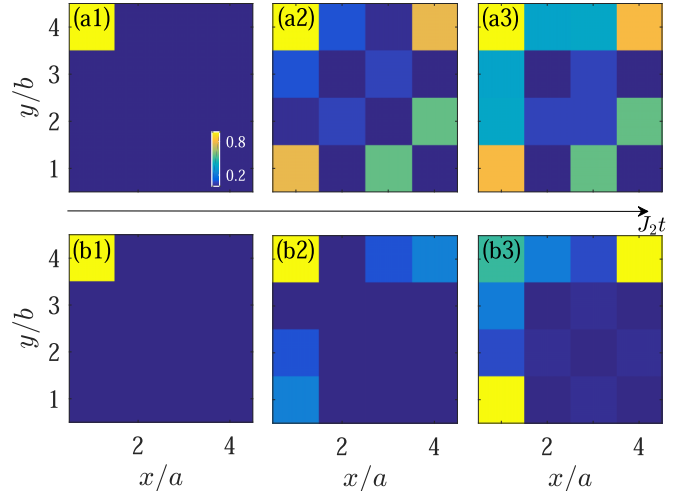


FIG. 5. Time evolutions of single-excitation state population at the upper-left qubit ($Q_{4,1}$). (a1)–(a3) The time evolutions of the probability distributions with $J_1/J_2 = 1.2$ for $J_2t = 0, 10$, and 20 , respectively. (b1)–(b3) The same evolutions but with $J_1/J_2 = 0.2$. Here $N = 4$.

trum of the midgap modes. As shown in Fig. 6(b), the four modes are grouped into two degenerate pairs with eigenenergies E_\pm due to the finite lattice size effect. Specifically,

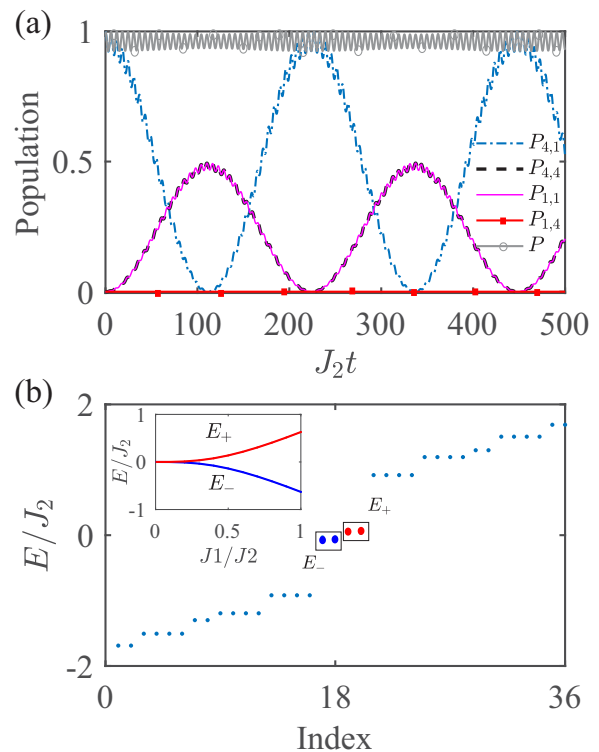


FIG. 6. (a) Time evolution of the population of the four localized corner qubits ($P_{4,1}$, $P_{4,4}$, $P_{1,1}$, $P_{1,4}$). $P = \sum P_{i,j}$ ($i, j = 1, 4$). (b) Energy spectrum with $J_1/J_2 = 0.1$. The inset graph shows the eigenvalue as a function of J_1/J_2 . E_- and E_+ are the eigenvalues of the two-pair degenerate midgap states.

for a 4×4 qubit lattice, these states can be respectively expressed as

$$|\varphi_{1,-}\rangle = -\lambda_1|\Psi_{4,4}\rangle + \lambda_1|\Psi_{1,1}\rangle - \lambda_2|\Psi_{1,4}\rangle, \quad (22)$$

$$|\varphi_{2,-}\rangle = \lambda_2|\Psi_{4,1}\rangle + \lambda_1|\Psi_{4,4}\rangle + \lambda_1|\Psi_{1,1}\rangle, \quad (23)$$

$$|\varphi_{1,+}\rangle = -\lambda_1|\Psi_{4,4}\rangle + \lambda_1|\Psi_{1,1}\rangle + \lambda_2|\Psi_{1,4}\rangle, \quad (24)$$

$$|\varphi_{2,+}\rangle = \lambda_2|\Psi_{4,1}\rangle - \lambda_1|\Psi_{4,4}\rangle - \lambda_1|\Psi_{1,1}\rangle, \quad (25)$$

where $\lambda_{1,2}$ are the positive coefficients with $\lambda_2 = \sqrt{2}\lambda_1$, and $|\varphi_{s,+}\rangle$ ($|\varphi_{s,-}\rangle$) corresponds to E_+ (E_-), with $E_{\pm} = \pm\sqrt{2J_1^2 + J_2^2 - J_2\sqrt{4J_1^2 + J_2^2}}$ and $s = 1, 2$. The energy splitting between E_+ and E_- plays a crucial role in the qubit flipping dynamics among corners. Supposing the initial state is localized at the bottom-right corner, $|\psi(0)\rangle = |\Psi_{4,1}\rangle$, the time-dependent quantum state is then described by

$$|\psi(t)\rangle = \frac{1}{2\lambda_2}(e^{-iE_+t}|\varphi_{2,+}\rangle + e^{-iE_-t}|\varphi_{2,-}\rangle). \quad (26)$$

According to Eq. (26), the excited-state populations of the four corners are obtained respectively as $P_{1,4} = |\langle\Psi_{1,4}|\psi(t)\rangle|^2 = 0$, $P_{1,1} = |\langle\Psi_{1,1}|\psi(t)\rangle|^2 = [1 - \cos(\omega_0 t)]/4$, $P_{4,4} = |\langle\Psi_{4,4}|\psi(t)\rangle|^2 = [1 - \cos(\omega_0 t)]/4$, and $P_{4,1} = |\langle\Psi_{4,1}|\psi(t)\rangle|^2 = [1 + \cos(\omega_0 t)]/2$ with $\omega_0 = E_+ - E_-$. This explains the periodic oscillation among the three corners.

B. Corner state transfer

The topological midgap modes discussed above provide an instructive way to transfer the quantum state encoded in lattice corners. In the following we show the protocol of state transfer between two diagonal lattice corners ($Q_{4,1}$ and $Q_{1,4}$). To see how it works, it is convenient to move into a newly defined frame, where

$$|\Psi_+\rangle = (|\Psi_{4,4}\rangle + |\Psi_{1,1}\rangle)/\sqrt{2}, \quad (27)$$

$$|\Psi_-\rangle = (|\Psi_{4,4}\rangle - |\Psi_{1,1}\rangle)/\sqrt{2}, \quad (28)$$

and therefore Eqs. (22)–(25) become

$$|\varphi_{1,-}\rangle = -\lambda_2|\Psi_{1,4}\rangle - \sqrt{2}\lambda_1|\Psi_-\rangle, \quad (29)$$

$$|\varphi_{2,-}\rangle = \lambda_2|\Psi_{4,1}\rangle + \sqrt{2}\lambda_1|\Psi_+\rangle, \quad (30)$$

$$|\varphi_{1,+}\rangle = \lambda_2|\Psi_{1,4}\rangle - \sqrt{2}\lambda_1|\Psi_-\rangle, \quad (31)$$

$$|\varphi_{2,+}\rangle = \lambda_2|\Psi_{4,1}\rangle - \sqrt{2}\lambda_1|\Psi_+\rangle. \quad (32)$$

While the lack of a coupling channel prohibits the direct state transfer between $|\Psi_{4,1}\rangle$ and $|\Psi_{1,4}\rangle$, the state $|\Psi_{4,1}\rangle$ ($|\Psi_{1,4}\rangle$) couples to $|\Psi_+\rangle$ ($|\Psi_-\rangle$) through Rabi-like oscillation, as schematically shown in Fig. 7. An auxiliary channel between $|\Psi_+\rangle$ and $|\Psi_-\rangle$ might be a promising way to bridge $|\Psi_{4,1}\rangle$ with $|\Psi_{1,4}\rangle$. This could be possible if we impose onsite potentials on the lattice corners. By doing so, the Hamiltonian becomes an external-potential-dependent

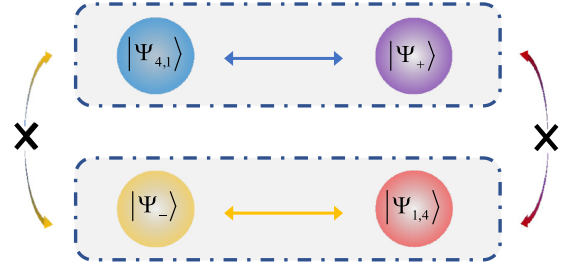


FIG. 7. Schematic diagram of the couplings between $|\Psi_{4,1}\rangle$, $|\Psi_{1,4}\rangle$, and $|\Psi_{\pm}\rangle$ according to Eqs. (29)–(32).

form, i.e.,

$$H'(\delta'_1, \delta'_2) = H + \delta'_1(\sigma_{4,4}^+ \sigma_{4,4}^- - \sigma_{1,1}^+ \sigma_{1,1}^-) + \delta'_2(\sigma_{4,1}^+ \sigma_{4,1}^- - \sigma_{1,4}^+ \sigma_{1,4}^-). \quad (33)$$

In Eq. (33), δ'_1 and δ'_2 are the controllable parameters, either of which may lift the twofold degeneracy of the midgap modes $|\varphi_{1,\pm}\rangle$ and $|\varphi_{2,\pm}\rangle$ with modified eigenenergies $E_{1,\pm}$ and $E_{2,\pm}$, respectively, as shown in Figs. 8(a) and 8(b). Before showing the details of the full quantum dynamics, it is beneficial to specify the roles of δ'_1 and δ'_2 . Figures 8(c) and 8(d) show the spin populations of the four midgap modes for systems with $H'(\delta'_1 \neq 0, \delta'_2 = 0)$ and $H'(\delta'_1 = 0, \delta'_2 \neq 0)$, respectively. It can be seen that by switching the onsite potentials, the eigenmodes $|\varphi_{n,\pm}\rangle$ can be reduced to certain basis $|\Psi_{i,j}\rangle$. With this understanding we are motivated to properly engineer δ'_1 and δ'_2 to transfer a space-localized quantum state in a dynamical manner. Assuming the initial state is $|\psi(t=0)\rangle = |\Psi_{1,4}\rangle$, we let it evolve under the free Hamiltonian \tilde{H}_{eff} until $t = T_1 \equiv \pi/\omega_0$, at which time we

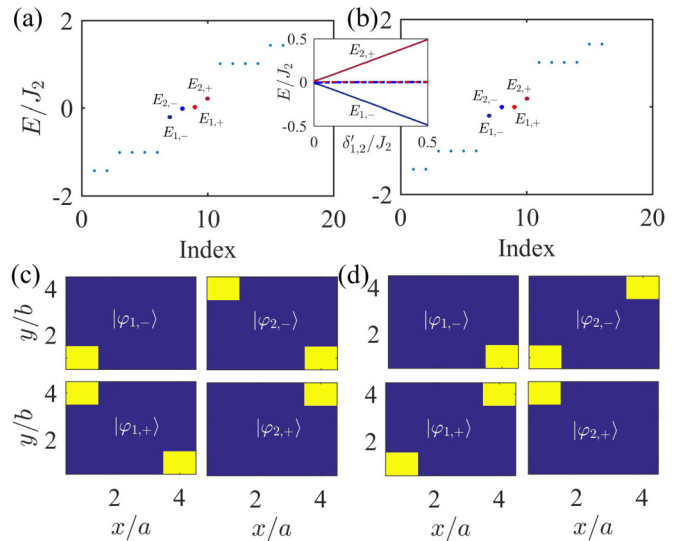


FIG. 8. Energy spectra with $\{\delta'_1/J_2 = 0.2, \delta'_2/J_2 = 0\}$ (a) and $\{\delta'_1/J_2 = 0, \delta'_2/J_2 = 0.2\}$ (b), respectively. The inset graph shows the four mid gap energies as a function of δ'_1 (δ'_2). (c), (d) State population of the four midgap corner modes corresponding to (a) and (b), respectively. The other parameters are $J_1/J_2 = 0.1$ and $N = 4$.

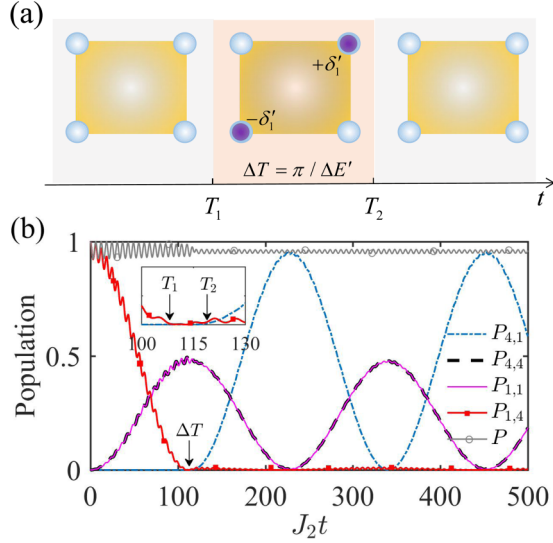


FIG. 9. (a) Schematic description of the configurations through quench dynamics. (b) Time evolution of the population of the four localized corner qubits. The other parameters are $J_1/J_2 = 0.1$, $\delta'_1/J_2 = 0.2$. (Inset) Closeup of the population at around $\Delta T = T_2 - T_1$.

turn on the on-site potential δ'_1 and hold it for a duration time $\Delta T = \pi / \Delta E'$ with $\Delta E' = E_{1,-} - E_{2,+}$ [this process is shown in Fig. 9(a)]. The qubit oscillates between $|\Psi_{1,4}\rangle$ and $|\Psi_{-}\rangle$ with period $2\pi / \omega_0$ if no further operation is performed [see Fig. 9(b)]. To freeze the target quantum state to the lattice corner $Q_{1,4}$ permanently, one can apply the potential δ'_2 at time $t = T_3 = T_1 + T_2$, as shown in Fig. 10(a). The full process is controlled by the following time-dependent

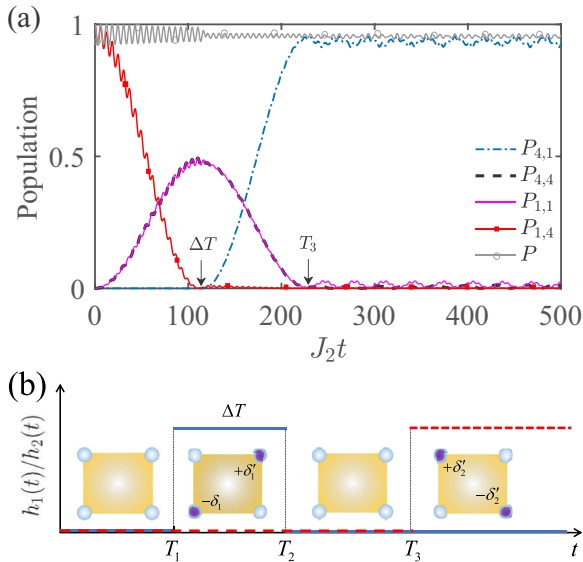


FIG. 10. (a) Time evolution of the population of the four localized corner qubits. (b) Timing of the quench dynamics. The blue-solid (red-dashed) curve denotes $h_1(t)$ [$h_2(t)$]. The other parameters are $J_1/J_2 = 0.1$, $\delta'_1/J_2 = \delta'_2/J_2 = 0.2$.

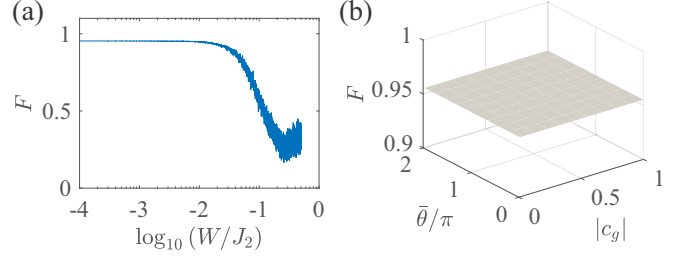


FIG. 11. (a) The fidelity of the corner state transfer vs the disorder coupling strength W . (b) The fidelity of the corner state transfer for arbitrary initial state with amplitude $|c_g|$ and relative phase $\bar{\theta}$. The other parameters are the same as those in Fig. 10(a).

Hamiltonian

$$H''(t) = H + h_1(t)(\sigma_{4,4}^+ \sigma_{4,4}^- - \sigma_{1,1}^+ \sigma_{1,1}^-) + h_2(t)(\sigma_{4,1}^+ \sigma_{4,1}^- - \sigma_{1,4}^+ \sigma_{1,4}^-), \quad (34)$$

where $h_1(t) = \delta'_1[\Theta(t - T_1) - \Theta(t - T_1 - \Delta T)]$ and $h_2(t) = \delta'_2\Theta(t - T_3)$, with $\Theta(t)$ being the step function. The sequential diagram of the quench dynamics is shown in Fig. 10(b).

To further verify the feasibility of the topological corner state transfer, we numerically calculate the fidelity $F = \langle \psi(0) | \psi(t_f) \rangle$ as a function of the imperfection strength. Figure 11(a) shows that there is a wide plateau at $F \approx 0.95$ when the disorder strength increases, which is a hallmark of the topologically assisted quantum state transfer. Additionally, for an arbitrary single-qubit initial state $|\psi(0)\rangle = |c_g|e^{i\bar{\theta}}|g\rangle + |c_e|e|e\rangle$ at one corner, where $|c_g|^2 + |c_e|^2 = 1$, the state can also be transferred with high fidelity, as shown in Fig. 11(b).

V. CONCLUSIONS

In summary, we have constructed a 2D BBH-type superconducting qubit lattice with tunable coupling strengths. As an example of a quadrupole higher-order topological insulator, such a model possesses topologically protected corner states. Through the nonequilibrium dynamics of a single-qubit excitation state, we showed that the quadrupole topological phases can be characterized by a dynamical dependent quantity, which takes zero for the trivial quadrupole phase and a finite value for the nontrivial quadrupole phase. The robustness of the quadrupole phases against disorder is also demonstrated. Moreover, we have demonstrated an effective scheme to realize the topological corner state transfer. In the experiment, accurate single-shot readout techniques enable us to synchronously record the dynamics of all qubits and to observe the evolution of a single-excitation state. In addition, the physics presented here persists even for a 4×4 lattice, indicating the feasibility of experimental measurements. Note that since multiple-qubit excitations can be precisely prepared in our system, it is interesting to further study interacting symmetry-protected higher-order topological states. Our work potentially paves the way for studying novel topological states of matter in controllable supercon-

ducting qubit systems and may shed light on the ongoing research of topologically protected quantum information processing.

ACKNOWLEDGMENTS

This work is supported partly by the NSFC under Grants No. 12034012, No. 12074232, No. 11804204, and No. 1331KSC.

APPENDIX: THE MCD FOR DIFFERENT INITIAL STATES

In the main text (Sec. III), we numerically calculate $C_1^{r_x+1, r_y}(t) + C_3^{r_x, r_y+1}(t)$, which can effectively characterize the quadrupole topological phases. Same results can be obtained by choosing $C_2^{r_x, r_y}(t) + C_4^{r_x+1, r_y+1}(t)$. Here we study the impacts of other different initial states imposed on the MCD. In the limiting case ($J_1 \neq 0, J_2 = 0$), the MCD can be analytically obtained as $C_{\text{total}}^{\text{triv}}(t) \sim \cos 2\sqrt{2}t$, which is independent of the initial state. Although the analytical results for more general topological trivial cases are inaccessible, we can still numerically verify that $\bar{C}_{\text{total}} = 0$. In the following we focus on the nontrivial case ($J_1/J_2 < 1$).

As examples we consider the qubit lattice with $N = 6$ and study three cases—case I for $C_{\text{total}}(t) = C_2^{1,1}(t) + C_3^{2,1}(t)$,

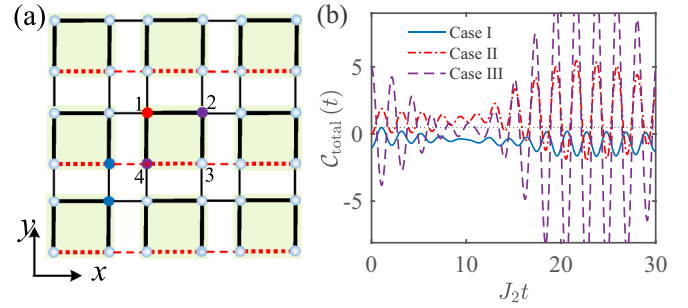


FIG. 12. (a) Schematic of qubit lattice in unit-cell coordinate with different initial state. Case I (blue shade) denotes the two initial states localized at $[(1, 1), 2]$ and $[(2, 1), 3]$, respectively. Case II (red shade) denotes the two initial states localized at $[(2, 2), 1]$ and $[(2, 2), 4]$, respectively. Case III (purple shade) denotes the two initial states localized at $[(2, 2), 2]$ and $[(2, 2), 4]$, respectively. (b) The dynamics of $C_{\text{total}}(t)$ with different initial states. Here $N = 6$, and $J_1/J_2 = 0.2$.

case II for $C_{\text{total}}(t) = C_1^{2,2}(t) + C_4^{2,2}(t)$, and case III for $C_{\text{total}}(t) = C_2^{2,2}(t) + C_4^{2,2}(t)$, as shown in Fig. 12(a). Figure 12(b) shows the dynamics of $C_{\text{total}}(t)$ under these cases. The results indicate that $C_{\text{total}}(t)$ does not oscillate around a certain value and $\bar{C}_{\text{total}} \neq 0.5$.

-
- [1] J. Koch, T. M. Yu, J. Gambetta, A. A. Houck, D. I. Schuster, J. Majer, A. Blais, M. H. Devoret, S. M. Girvin, and R. J. Schoelkopf, Charge-insensitive qubit design derived from the Cooper pair box, *Phys. Rev. A* **76**, 042319 (2007).
- [2] X. Gu, A. F. Kockum, A. Miranowicz, Y. Liu, and F. Nori, Microwave photonics with superconducting quantum circuits, *Phys. Rep.* **718-719**, 1 (2017).
- [3] A. A. Houck, H. E. Tüeci, and J. Koch, On-chip quantum simulation with superconducting circuits, *Nat. Phys.* **8**, 292 (2012).
- [4] I. M. Georgescu, S. Ashhab, and F. Nori, Quantum simulation, *Rev. Mod. Phys.* **86**, 153 (2014).
- [5] M. J. Hartmann, Quantum simulation with interacting photons, *J. Opt.* **18**, 104005 (2016).
- [6] D.-W. Zhang, Y.-Q. Zhu, Y. X. Zhao, H. Yan, and S.-L. Zhu, Topological quantum matter with cold atoms, *Adv. Phys.* **67**, 253 (2019).
- [7] T. Ozawa, H. M. Price, A. Amo, N. Goldman, M. Hafezi, L. Lu, M. C. Rechtsman, D. Schuster, J. Simon, O. Zilberberg, and I. Carusotto, Topological photonics, *Rev. Mod. Phys.* **91**, 015006 (2019).
- [8] J. Jin, D. Rossini, R. Fazio, M. Leib, and M. J. Hartmann, Photon Solid Phases in Driven Arrays of Nonlinearly Coupled Cavities, *Phys. Rev. Lett.* **110**, 163605 (2013).
- [9] M. Kounalakis, C. Dickel, A. Bruno, N. K. Langford, and G. A. Steele, Tuneable hopping and nonlinear cross-Kerr interactions in a high-coherence superconducting circuit, *npj Quantum Inf.* **4**, 38 (2018).
- [10] Y. Ye, Z.-Y. Ge, Y. Wu, S. Wang, M. Gong, Y.-R. Zhang, Q. Zhu, R. Yang, S. Li, F. Liang, J. Lin, Y. Xu, C. Guo, L. Sun, C. Cheng, N. Ma, Z. Y. Meng, H. Deng, H. Rong, C.-Y. Lu, C.-Z. Peng, H. Fan, X. Zhu, and J.-W. Pan, Propagation and Localization of Collective Excitations on a 24-Qubit Superconducting Processor, *Phys. Rev. Lett.* **123**, 050502 (2019).
- [11] P. Roushan, C. Neill, J. Tangpanitanon, V. M. Bastidas, A. Megrant, R. Barends, Y. Chen, Z. Chen, B. Chiaro, A. Dunsworth, A. Fowler, B. Foxen, M. Giustina, E. Jeffrey, J. Kelly, E. Lucero, J. Mutus, M. Neeley, C. Quintana, D. Sank, A. Vainsencher, J. Wenner, T. White, H. Neven, D. G. Angelakis, and J. Martinis, Spectroscopic signatures of localization with interacting photons in superconducting qubits, *Science* **358**, 1175 (2017).
- [12] K. Xu, J.-J. Chen, Y. Zeng, Y.-R. Zhang, C. Song, W. Liu, Q. Guo, P. Zhang, D. Xu, H. Deng, K. Huang, H. Wang, X. Zhu, D. Zheng, and H. Fan, Emulating Many-Body Localization with a Superconducting Quantum Processor, *Phys. Rev. Lett.* **120**, 050507 (2018).
- [13] T. Orell, A. A. Michailidis, M. Serbyn, and M. Silveri, Probing the many-body localization phase transition with superconducting circuits, *Phys. Rev. B* **100**, 134504 (2019).
- [14] Q. Guo, C. Cheng, Z. Sun, Z. Song, H. Li, Z. Wang, W. Ren, H. Dong, D. Zheng, Y.-R. Zhang, R. Mondaini, H. Fan, and H. Wang, Observation of energy-resolved many-body localization, *Nat. Phys.* **17**, 234 (2020).
- [15] K. Xu, Z.-H. Sun, W. Liu, Y.-R. Zhang, H. Li, H. Dong, W. Ren, P. Zhang, F. Nori, D. Zheng, H. Fan, and H. Wang, Probing dynamical phase transitions with a superconducting quantum simulator, *Sci. Adv.* **6**, eaba4935 (2020).
- [16] V. V. Ramasesh, E. Flurin, M. Rudner, I. Siddiqi, and N. Y. Yao, Direct Probe of Topological Invariants Using Bloch Oscillating Quantum Walks, *Phys. Rev. Lett.* **118**, 130501 (2017).

- [17] E. Flurin, V. V. Ramasesh, S. Hacothen-Gourgy, L. S. Martin, N. Y. Yao, and I. Siddiqi, Observing Topological Invariants Using Quantum Walks in Superconducting Circuits, *Phys. Rev. X* **7**, 031023 (2017).
- [18] F. Mei, G. Chen, L. Tian, S.-L. Zhu, and S. Jia, Topology-dependent quantum dynamics and entanglement-dependent topological pumping in superconducting qubit chains, *Phys. Rev. A* **98**, 032323 (2018).
- [19] F. Mei, G. Chen, L. Tian, S.-L. Zhu, and S. Jia, Robust quantum state transfer via topological edge states in superconducting qubit chains, *Phys. Rev. A* **98**, 012331 (2018).
- [20] L.-N. Zheng, L. Qi, L.-Y. Cheng, H.-F. Wang, and S. Zhang, Defect-induced controllable quantum state transfer via a topologically protected channel in a flux qubit chain, *Phys. Rev. A* **102**, 012606 (2020).
- [21] P. Roushan, C. Neill, Y. Chen, M. Kolodrubetz, C. Quintana, N. Leung, M. Fang, R. Barends, B. Campbell, Z. Chen, B. Chiaro, A. Dunsworth, E. Jeffrey, J. Kelly, A. Megrant, J. Mutus, P. J. J. O'Malley, D. Sank, A. Vainsencher, J. Wenner, T. White, A. Polkovnikov, A. N. Cleland, and J. M. Martinis, Observation of topological transitions in interacting quantum circuits, *Nature (London)* **515**, 241 (2014).
- [22] W. Nie and Y.-x. Liu, Bandgap-assisted quantum control of topological edge states in a cavity, *Phys. Rev. Research* **2**, 012076(R) (2020).
- [23] J. Niu, T. Yan, Y. Zhou, Z. Tao, X. Li, W. Liu, L. Zhang, S. Liu, Z. Yan, Y. Chen, and D. Yu, Simulation of higher-order topological phases and related topological phase transitions in a superconducting qubit, *Sci. Bull.* **66**, 1168 (2021).
- [24] W. Cai, J. Han, F. Mei, Y. Xu, Y. Ma, X. Li, H. Wang, Y. P. Song, Z.-Y. Xue, Z.-q. Yin, S. Jia, and L. Sun, Observation of Topological Magnon Insulator States in a Superconducting Circuit, *Phys. Rev. Lett.* **123**, 080501 (2019).
- [25] M. Gong, S. Wang, C. Zha, M.-C. Chen, H.-L. Huang, Y. Wu, Q. Zhu, Y. Zhao, S. Li, S. Guo, H. Qian, Y. Ye, F. Chen, C. Ying, J. Yu, D. Fan, D. Wu, H. Su, H. Deng, H. Rong, K. Zhang, S. Cao, J. Lin, Y. Xu, L. Sun, C. Guo, N. Li, F. Liang, V. M. Bastidas, K. Nemoto, W. J. Munro, Y.-H. Huo, C.-Y. Lu, C.-Z. Peng, X. Zhu, and J.-W. Pan, Quantum walks on a programmable two-dimensional 62-qubit superconducting processor, *Science* **372**, 948 (2021).
- [26] Y.-P. Wang, W.-L. Yang, Y. Hu, Z.-Y. Xue, and Y. Wu, Detecting topological phases of microwave photons in a circuit quantum electrodynamics lattice, *npj Quantum Inf.* **2**, 16015 (2016).
- [27] C. Owens, A. LaChapelle, B. Saxberg, B. M. Anderson, R. Ma, J. Simon, and D. I. Schuster, Quarter-flux Hofstadter lattice in a qubit-compatible microwave cavity array, *Phys. Rev. A* **97**, 013818 (2018).
- [28] A. D. King, J. Carrasquilla, J. Raymond, I. Ozfidan, E. Andriyash, A. Berkley, M. Reis, T. Lanting, R. Harris, F. Altomare, K. Boothby, P. I. Bunyk, C. Enderud, A. Fréchet, E. Hoskinson, N. Ladizinsky, T. Oh, G. Poulin-Lamarre, C. Rich, Y. Sato, A. Y. Smirnov, L. J. Swenson, M. H. Volkman, J. Whittaker, J. Yao, E. Ladizinsky, M. W. Johnson, J. Hilton, and M. H. Amin, Observation of topological phenomena in a programmable lattice of 1, 800 qubits, *Nature (London)* **560**, 456 (2018).
- [29] Y. Yanay, J. Braumüller, S. Gustavsson, W. D. Oliver, and C. Tahan, Two-dimensional hard-core Bose-Hubbard model with superconducting qubits, *npj Quantum Inf.* **6**, 58 (2020).
- [30] T. Chen and Z.-Y. Xue, Nonadiabatic Geometric Quantum Computation with Parametrically Tunable Coupling, *Phys. Rev. Appl.* **10**, 054051 (2018).
- [31] T. Chen, P. Shen, and Z.-Y. Xue, Robust and Fast Holonomic Quantum Gates with Encoding on Superconducting Circuits, *Phys. Rev. Appl.* **14**, 034038 (2020).
- [32] M. Z. Hasan and C. L. Kane, Colloquium: Topological insulators, *Rev. Mod. Phys.* **82**, 3045 (2010).
- [33] X.-L. Qi and S.-C. Zhang, Topological insulators and superconductors, *Rev. Mod. Phys.* **83**, 1057 (2011).
- [34] W. A. Benalcazar, B. A. Bernevig, and T. L. Hughes, Quantized electric multipole insulators, *Science* **357**, 61 (2017).
- [35] W. A. Benalcazar, B. A. Bernevig, and T. L. Hughes, Electric multipole moments, topological multipole moment pumping, and chiral hinge states in crystalline insulators, *Phys. Rev. B* **96**, 245115 (2017).
- [36] F. Schindler, A. M. Cook, M. G. Vergniory, Z. Wang, S. S. P. Parkin, B. A. Bernevig, and T. Neupert, Higher-order topological insulators, *Sci. Adv.* **4**, eaat0346 (2018).
- [37] M. Serra-Garcia, V. Peri, R. Süstrunk, O. R. Bilal, T. Larsen, L. G. Villanueva, and S. D. Huber, Observation of a phononic quadrupole topological insulator, *Nature (London)* **555**, 342 (2018).
- [38] C. W. Peterson, W. A. Benalcazar, T. L. Hughes, and G. Bahl, A quantized microwave quadrupole insulator with topologically protected corner states, *Nature (London)* **555**, 346 (2018).
- [39] B.-Y. Xie, H.-F. Wang, H.-X. Wang, X.-Y. Zhu, J.-H. Jiang, M.-H. Lu, and Y.-F. Chen, Second-order photonic topological insulator with corner states, *Phys. Rev. B* **98**, 205147 (2018).
- [40] S. Mittal, V. V. Orre, G. Zhu, M. A. Gorlach, A. Poddubny, and M. Hafezi, Photonic quadrupole topological phases, *Nat. Photonics* **13**, 692 (2019).
- [41] X. Ni, M. Weiner, A. Alú, and A. B. Khanikaev, Observation of higher-order topological acoustic states protected by generalized chiral symmetry, *Nat. Mater.* **18**, 113 (2019).
- [42] H. Xue, Y. Yang, F. Gao, Y. Chong, and B. Zhang, Acoustic higher-order topological insulator on a kagome lattice, *Nat. Mater.* **18**, 108 (2019).
- [43] Q. Wei, X. Zhang, W. Deng, J. Lu, X. Huang, M. Yan, G. Chen, Z. Liu, and S. Jia, Higher-order topological semimetal in acoustic crystals, *Nat. Mater.* **20**, 812 (2021).
- [44] W. Zhang, X. Xie, H. Hao, J. Dang, S. Xiao, S. Shi, H. Ni, Z. Niu, C. Wang, K. Jin, X. Zhang, and X. Xu, Low-threshold topological nanolasers based on the second-order corner state, *Light Sci. Appl.* **9**, 109 (2020).
- [45] R. W. Bomantara and J. Gong, Measurement-only quantum computation with Floquet Majorana corner modes, *Phys. Rev. B* **101**, 085401 (2020).
- [46] C.-H. Hsu, P. Stano, J. Klinovaja, and D. Loss, Majorana Kramers Pairs in Higher-Order Topological Insulators, *Phys. Rev. Lett.* **121**, 196801 (2018).
- [47] T. Liu, J. J. He, and F. Nori, Majorana corner states in a two-dimensional magnetic topological insulator on a high-temperature superconductor, *Phys. Rev. B* **98**, 245413 (2018).
- [48] S. Caldwell, N. Didier, C. A. Ryan, E. A. Sete, A. Hudson, P. Karalekas, R. Manenti, M. P. da Silva, R. Sinclair, and E. Acala, Parametrically Activated Entangling Gates Using Transmon Qubits, *Phys. Rev. Appl.* **10**, 034050 (2018).
- [49] X. Li, Y. Ma, J. Han, T. Chen, Y. Xu, W. Cai, H. Wang, Y. P. Song, Z.-Y. Xue, Z.-Q. Yin, and L. Sun, Perfect Quantum State

- Transfer in a Superconducting Qubit Chain with Parametrically Tunable Couplings, *Phys. Rev. Appl.* **10**, 054009 (2018).
- [50] M. Reagor, C. B. Osborn, N. Tezak, A. Staley, G. Prawiroatmodjo, M. Scheer, N. Alidoust, E. A. Sete, N. Didier, and M. P. da Silva, Demonstration of universal parametric entangling gates on a multi-qubit lattice, *Sci. Adv.* **4**, eaao3603 (2018).
- [51] H. Alaeian, C. W. S. Chang, M. V. Mghaddam, C. M. Wilson, E. Solano, and E. Rico, Creating lattice gauge potentials in circuit QED: The bosonic Creutz ladder, *Phys. Rev. A* **99**, 053834 (2019).
- [52] X. Guan, Y. Feng, Z.-Y. Xue, G. Chen, and Suotang Jia, Synthetic gauge field and chiral physics on two-leg superconducting circuits, *Phys. Rev. A* **102**, 032610 (2020).
- [53] F. Liu and K. Wakabayashi, Novel Topological Phase with a Zero Berry Curvature, *Phys. Rev. Lett.* **118**, 076803 (2017).
- [54] L.-Y. Zheng, V. Achilleos, O. Richoux, G. Theoharis, and V. Pagneux, Observation of Edge Waves in a Two-Dimensional Su-Schrieffer-Heeger Acoustic Network, *Phys. Rev. Appl.* **12**, 034014 (2019).
- [55] Y. Meng, G. Chen, and S. Jia, Second-order topological insulator in a coinless discrete-time quantum walk, *Phys. Rev. A* **102**, 012203 (2020).
- [56] M. Maffei, A. Dauphin, F. Cardano, M. Lewenstein, and P. Massignan, Topological characterization of chiral models through their long time dynamics, *New J. Phys.* **20**, 013023 (2018).
- [57] F. Cardano, A. D'Errico, A. Dauphin, M. Maffei, B. Piccirillo, C. de Lisio, G. D. Filippis, V. Cataudella, E. Santamato, L. Marrucci, M. Lewenstein, and P. Massignan, Detection of Zak phases and topological invariants in a chiral quantum walk of twisted photons, *Nat. Commun.* **8**, 15516 (2017).
- [58] E. J. Meier, F. A. An, A. Dauphin, M. Maffei, P. Massignan, T. L. Hughes, and B. Gadway, Observation of the topological Anderson insulator in disordered atomic wires, *Science* **362**, 929 (2018).
- [59] T. Mizoguchi, Y. Kuno, and Y. Hatsugai, Detecting Bulk Topology of Quadrupolar Phase from Quench Dynamics, *Phys. Rev. Lett.* **126**, 016802 (2021).